mathematics

MDPI

Article

Sub-Mesoscale Frontal Instabilities in the Omani Coastal Current

Mathieu Morvan *,† **and Xavier Carton** †

Laboratoire d'Océanographie Physique et Spatiale, UMR 6523 Univ. Brest-CNRS-IFREMER-IRD, Institut Universitaire Européen de la Mer, rue Dumont d'Urville, 29280 Plouzané, France; xcarton@univ-brest.fr

* Correspondence: mmorvan3@univ-brest.fr

† Current address: Institut Universitaire Européen de la Mer, rue Dumont d'Urville, 29280 Plouzané, France.

Received: 13 February 2020; Accepted: 7 April 2020; Published: 11 April 2020

Abstract: The Omani Coastal Current (OCC) flowing northward along the southern coast of Oman during the summer monsoon is associated with an upwelling system. The mesoscale circulation of the western Arabian Sea is dominated by energetic mesoscale eddies down to about 1000 m depth. They drive the pathways of the upwelling water masses and the Persian Gulf Outflow water. This paper focuses on the sub-mesoscale frontal dynamics in the OCC by analyzing the results from a regional realistic numerical simulation performed with a primitive equation model. Off the Omani coast, the interaction between the upwelling fronts and the mesoscale eddies triggers the frontogenesis at play in the surface mixed layer during the summer monsoon. In spring, sub-mesoscale eddies are generated at the Cape of Ra's al Hadd due to the horizontal shear instabilities undergone by the OCC. The OCC also drives and elongates Peddies formed during the Summer monsoon and located below the thermocline. Finally, the interaction between mesoscale eddies and the upwelling system leads to the formation of sub-mesoscale eddies at depth through baroclinic instabilities.

Keywords: sub-mesoscale; fronts; instabilities

1. Introduction

The regional-scale ocean circulation in the Arabian Sea, the north-western part of the Indian Ocean, is driven by the winter and the summer monsoons [1]. During the winter monsoon, the winds blow from the North-East to the south-west direction inducing a cyclonic gyre circulation. In contrast, the regional circulation during the summer monsoon is dominated by an anticyclonic gyre due to the intense wind that is oriented northeastward (and blows on average at about 14 m s^{-1}, [2]). On the one hand, the offshore (onshore) Ekman transport due to the orientation of the wind generates upwelling (downwelling) in summer (winter) [3]. On the other hand, both monsoon regimes lead to the formation of a coastal current along the southern coast of Oman, flowing northward (southward) in summer (winter) named the Omani Coastal Current (OCC). When arriving near the Cape of Ra's al Hadd, the summer OCC becomes the Ra's al Hadd jet characterized by the formation of the Ra's al Hadd dipole with intense horizontal velocity (up to about 1 m s^{-1} [4]). By the presence of, for instance, the Ra's al Hadd dipole and the cyclone off the Cape of Ra's Ash Sharbatat [4], the western Arabian Sea is home to an energetic mesoscale eddy field [5]. From May to September, off the Omani southern coast, mesoscale eddies are generated via the instability undergone by the OCC [6]. The OCC dynamics play an important role on the fate of the Persian Gulf Outflow Water (PGOW). PGOW is formed in the Persian Gulf via evaporation due to the strong solar radiation [7]. PGOW is a warm and salty, thus dense water [8]. PGOW enters the Gulf of Oman from the Persian Gulf via the Strait of Hormuz. Then, PGOW spreads at intermediate depths [9] (between 250–300 m depth) under the influence of deep mesoscale eddies [10,11]. Filaments of PGOW around the eddy rims which eventually break into

sub-mesoscale eddies have been measured far from the Strait of Hormuz by [12] off the Cape of Ra's al Hadd during the spring intermonsoon 2011.

In the world's ocean, the sub-mesoscale dynamics associated with western boundary current have been widely studied e.g., in the Gulf Stream [13–15], in the Kuroshio [16,17], and in the Agulhas Current [18,19]. However, OCC is more than a western boundary current since it is associated with an upwelling system during the summer monsoon. The sub-mesoscale dynamics associated with upwelling system have been investigated by [20–22] for the California Current System, and by [23] for the North-West African upwelling current.

This paper is dedicated to the sub-mesoscale frontal dynamics occurring in the Omani Coastal Current near the surface and at intermediate depths. It analyzes the results of a realistic regional simulation performed with a primitive equation model at sub-mesoscale resolution.

We present the model set-up and method in Section 2.4. Then, we analyze in detail the OCC, its filaments, the frontogenetic processes and the subsurface sub-mesoscale eddies in Section 3. The results are summarized in Section 4 and perspectives are proposed.

2. Model Equations and Numerical Set-Up

2.1. The Primitive Equations

The oceanic motions at horizontal scales larger than 1 km are well described by the primitive equations. Exceptions are convective motions with strong vertical accelerations and motions in a narrow equatorial band.

The primitive equations are the three-dimensional Navier–Stokes equations on a rotating planet, thus including the projection of the Earth rotation on the local vertical axis (the so-called traditional Coriolis component); the hydrostatic approximation is applied insofar as the horizontal scales of motion are much larger than the vertical scales (a few kilometers compared with a few meters). Finally, as the density in the ocean varies only by a few percent, it is commonplace to apply the Boussinesq approximation and thus to replace the term $(1/\rho)\boldsymbol{\nabla} p$ in the moment equations by $(1/\rho_0)\boldsymbol{\nabla} p$, where ρ_0 is the averaged density of oceanic waters.

Mathematically, the primitive equations are written, in a local Cartesian framework $(\boldsymbol{i}, \boldsymbol{j}, \boldsymbol{k})$ (West to East, South to North and bottom to top directions), at the surface of the Earth

$$\frac{Du}{Dt} + fv = \frac{-1}{\rho_0}\partial_x p + F_x^*/\rho_0 + A_h(\partial_x^2 + \partial_y^2)u + A_v\partial_z^2 u \tag{1}$$

$$\frac{Dv}{Dt} - fu = \frac{-1}{\rho_0}\partial_y p + F_y^*/\rho_0 + A_h(\partial_x^2 + \partial_y^2)v + A_v\partial_z^2 v \tag{2}$$

which are the two horizontal momentum equations in which F^* is the mechanical forcing,

$$0 = \frac{-1}{\rho_0}\partial_z p - \frac{\rho g}{\rho_0} \tag{3}$$

which is the hydrostatic equation, a simplification of the vertical momentum equation

$$\partial_x u + \partial_y v + \partial_z w = 0 \tag{4}$$

which is the incompressibility equation. In these equations, F_x^*, F_y^* are the volumic forces, A_h is a horizontal, and A_v a vertical turbulent viscosity. Indeed, in the ocean, the turbulent processes which govern mixing and dissipation do not have the same scales nor intensities horizontally and vertically.

Finally, since pressure and velocity are related via the momentum equations, and since pressure and density are related via the hydrostatic balance, another equation is needed to relate velocity and density; this is the buoyancy equation:

$$\frac{Db}{Dt} = B \tag{5}$$

where buoyancy b is $b = -g\rho/\rho_0$ with g the Earth gravity and B represents the buoyancy sources (via heat or freshwater fluxes).

In all these equations D/Dt is the material derivative using the three-dimensional velocity

$$D/Dt = \partial_t + u\partial_x + v\partial_y + w\partial_z \tag{6}$$

In the horizontal momentum equations, the last terms on the right-hand side can be gathered as total forces,

$$F_x^*/\rho_0 + A_h\nabla_h^2 u + A_z\partial_z^2 u = F_x/\rho_0\,, \tag{7}$$

$$F_y^*/\rho_0 + A_h\nabla_h^2 v + A_z\partial_z^2 v = F_y/\rho_0\,. \tag{8}$$

2.2. Vorticity and Potential Vorticity

By taking the curl of the horizontal momentum equations, one obtains a vorticity equation

$$\frac{D}{Dt}(\boldsymbol{\omega} + f\boldsymbol{k}) = (\boldsymbol{\omega} + f\boldsymbol{k})\cdot\boldsymbol{\nabla u} + \boldsymbol{\nabla}\times\boldsymbol{F/\rho_0} \tag{9}$$

with $\boldsymbol{\omega} = \boldsymbol{\nabla}\times\boldsymbol{u}$ the vorticity. In this vorticity vector, an important component for oceanic flows is vertical vorticity (also called relative vorticity)

$$\zeta = \omega_z = \partial_x v - \partial_y u \tag{10}$$

Taking the gradient of the buoyancy equation, one obtains

$$\frac{D}{Dt}\boldsymbol{\nabla} b = -\boldsymbol{\nabla} b\cdot\boldsymbol{\nabla u} + \boldsymbol{\nabla} B \tag{11}$$

Therefore, by multiplying the first equation by $\boldsymbol{\nabla} b$ and the second by $\boldsymbol{\omega} + f\boldsymbol{k}$, one obtains the evolution equation for potential vorticity $q = [\boldsymbol{\omega} + f\boldsymbol{k}]\cdot\boldsymbol{\nabla} b$

$$\boldsymbol{\frac{Dq}{Dt}} = \boldsymbol{\partial_t q + \nabla\cdot[uq] = \nabla\cdot[(\omega + fk)B - \nabla b\times F]} \tag{12}$$

using incompressibility (to obtain the flux of q).

2.3. Primitive Equation Model in Isopycnic Coordinates

The numerical model that we will use is the HYbrid Coordinate Ocean Model (HYCOM, [24]). It uses a hybrid vertical coordinates, a mix of geometrical coordinate z, geometrical coordinates scaled by the local water height h: $\sigma = z/h(x,y)$ and density (or isopycnic) coordinates ρ.

In these latter coordinates, the momentum equations of the primitive model acquire a particular form. Indeed, in the absence of forcing and of dissipation, they are written as

$$\frac{du}{dt} - fv = -\partial_x M \tag{13}$$

$$\frac{dv}{dt} + fu = -\partial_y M \tag{14}$$

where $M = \frac{p}{\rho} + gz$ is the Montgomery potential, $d/dt = \partial_t + (u\partial_x)|_\rho + (v\partial_y)|_\rho$, i.e., the "horizontal" velocities and derivatives are calculated along density surfaces. In this case, potential vorticity has the simple form

$$q = \frac{\zeta + f}{h_\rho} \tag{15}$$

where h_ρ is the distance between two successive isopycnals chosen for the vertical discretization.

2.4. Model Set-Up

A first simulation was performed at mesoscale resolution (∼5 km) covering the Arabian Sea, and including the adjacent evaporation basins (*viz* the Persian Gulf and the Red Sea), as shown in Figure 1a. The initialization, the surface and boundary forcings are described in [25]. The second simulation is a local zoom over the north-western Arabian Sea (see Figure 1b) performed with the Agrif method [26] at sub-mesoscale permitting resolution (∼1.5 km; remember that the first internal radius of deformation is about 50–60 km in this area). The Agrif zoom is a 1-way nest integration. 40 vertical levels non-equally spaced are used. The upper layer, from the surface down to 100 meters depth, is discretized with 20 vertical levels defined in z-coordinate; below, the water column is sampled by 20 vertical levels defined in isopycnic coordinates (see [25] for details). Re-analyzes of atmospheric forcings from the French meteorological office (Météo France) at $0.25^\circ \times 0.25^\circ$ resolution are used to force the ocean surface. The open boundaries are controlled by the first simulation mentioned above that includes 8 tidal modes from TOPEX data. The baroclinic and barotropic time steps are respectively 40 and 1 s. The vertical mixing is parameterized with a KPP-scheme [27]. Model viscosity is kept to a minimum compatible with numerical stability.

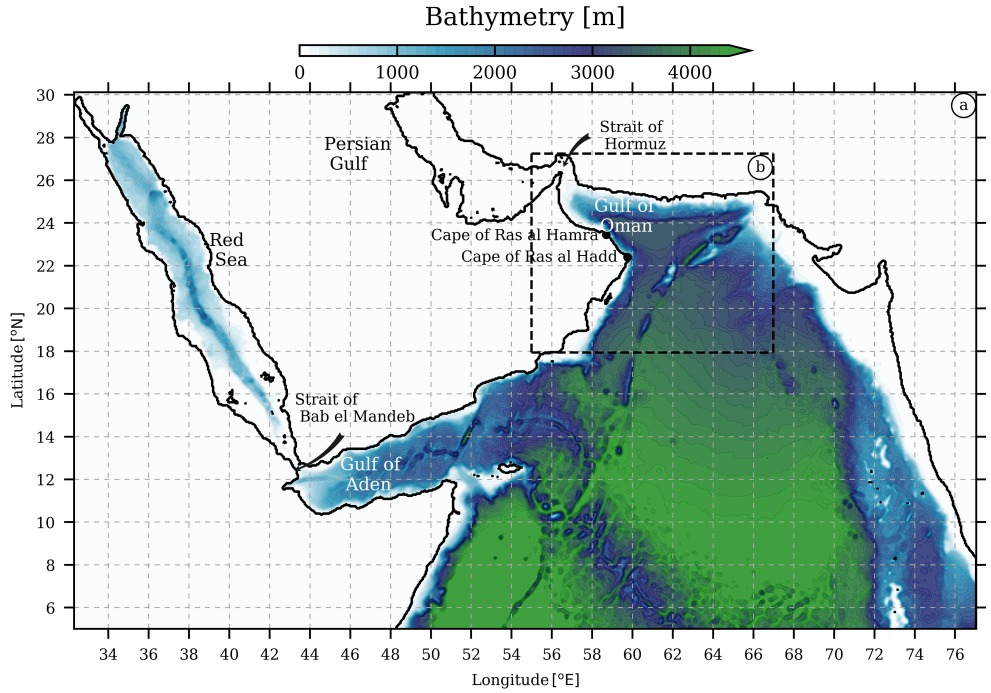

Figure 1. (**a**) Bathymetry of the Arabian Sea. (**b**) The domain used for the Agrif zoom is displayed in dashed black lines.

3. Results

3.1. The Occ and Sub-Mesoscale Upwelling Fronts

During the summer monsoon, the winds are oriented towards the North-East. Thus, the winds blow in the same direction as the south Omani coast generating a coastal upwelling system.

The temperature anomaly associated with the coastal upwelling system reaches -5 °C at 10 m depth, as shown in Figure 2a. The denser upwelled water facing offshore warmer water creates an upwelling front. Associated with this front is an alongshore current, the Omani Coastal Current (OCC). This current interacts with the eddy field offshore, so that its geometry becomes intricate with extrusions leaving the main current. In particular, the dense upwelled water is advected around the rims of mesoscale eddy located near the Omani coast (see the sea surface height contours in Figure 2a.). The along-front cold side is associated with high positive relative vorticity associated with intense vortex stretching. Furthermore, fine scale features are generated between the front and the mesoscale eddies (see insets of Figure 2a). High relative vorticity filaments oriented cross-front are associated with the fine scale features in temperature anomaly as shown in Figure 2b (insets). This suggests that sub-mesoscale frontal instabilities occur as the result of the interaction of the mesoscale eddies with the upwelling front.

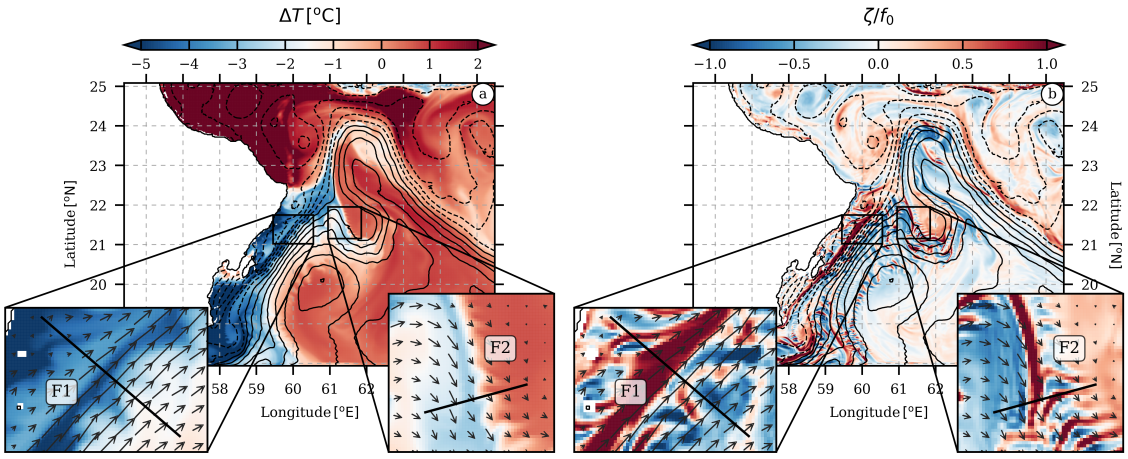

Figure 2. (**a**) Temperature anomaly and (**b**) surface relative vorticity normalized by the Coriolis frequency (f_0) during the south-west monsoon at 10 m depth. Black contours stand for the sea surface height anomaly. Surface velocity vectors are represented in insets.

From [28], the rate of density gradient intensification due to the straining induced by the velocity field can be diagnosed as:

$$F_s = \boldsymbol{Q} \cdot \boldsymbol{\nabla}_h \rho \,, \tag{16}$$

where

$$\boldsymbol{Q} = -\left(\partial_x u \partial_x \rho + \partial_x v \partial_y \rho,\, \partial_y u \partial_x \rho + \partial_y v \partial_y \rho\right) \,, \tag{17}$$

with u and v the zonal and meridional component of the velocity field, and ρ the density. F_s is shown in Figure 3. The maximal values of F_s are located along front and at sub-mesoscale, where ζ is large as expected from the frontogenesis theory [29]. Since the seasonal wind regime drives the upwelling system as well as the regional anticyclonic circulation of the Arabian Sea in summer, it is interesting to focus on the effect of the wind on the upwelling front intensification.

To do so, we start from the equation of the evolution of the (Ertel) potential vorticity [14], that is written as:

$$\partial_t q = -\boldsymbol{\nabla} \cdot \left(q\boldsymbol{u} - \boldsymbol{\omega}_a D_t b + \boldsymbol{\nabla} b \times \boldsymbol{F}\right) \,, \tag{18}$$

where $q = \boldsymbol{\omega}_a \cdot \boldsymbol{\nabla} b$ is the Ertel potential vorticity, $\boldsymbol{\omega}_a = f\boldsymbol{z} + \boldsymbol{\nabla} \times \boldsymbol{u}$ is the absolute vorticity, b the buoyancy, ρ_0 the mean density, and $\boldsymbol{F}$ is a vector that includes the non-conservative terms of the momentum equation. By neglecting the horizontal and the vertical dissipation, we can write:

$$\boldsymbol{F} \sim \frac{\boldsymbol{\tau}_w}{\rho_0 \delta z} \,, \tag{19}$$

with τ_w the wind stress, and δz the first layer thickness. Therefore, the potential vorticity flux injected by the wind can be diagnosed via $-\boldsymbol{\nabla} b \times \boldsymbol{\tau}_w / (\rho_0 \delta z)$ as shown in Figure 3b. The larger values are located where the buoyancy gradients are large, as expected. Moreover, destruction of potential vorticity can be due to the action of the downfront wind. The Ekman transport can then advect cold, dense, water above warm, lighter water, leading to static instability and mixing. In this region, potential vorticity can become negative, allowing the fronts to be symmetrically unstable [30].

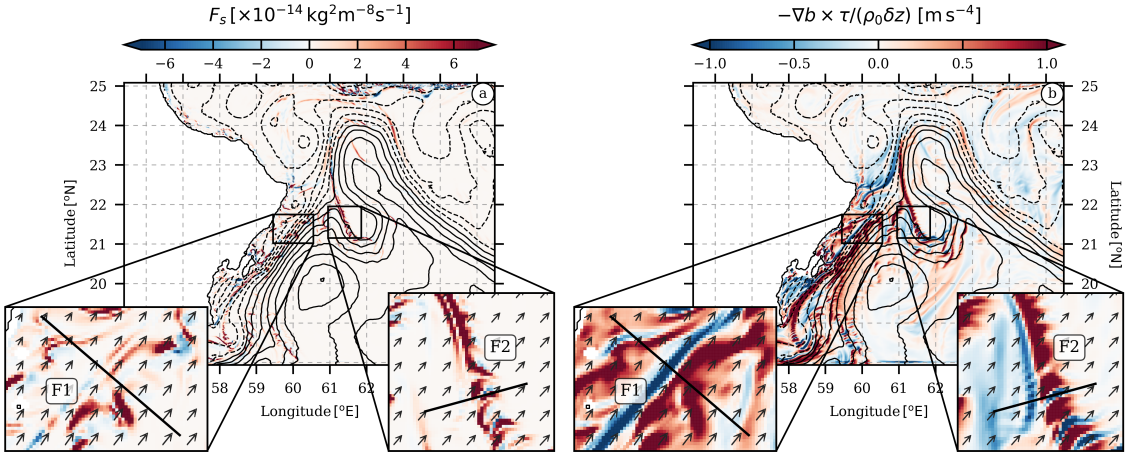

Figure 3. (**a**) Surface frontogenesis function and (**b**) the PV injection by the wind. The wind stress vectors are drawn in insets.

The vertical sections of the Ertel potential vorticity are shown in Figure 4a. Negative Ertel potential vorticity values locate in the surface mixed layer where the buoyancy gradient as well as the vertical gradient of horizontal velocity are strong. As mentioned above, the wind stress sustains the negative Ertel potential vorticity generation at the fronts induced by the interaction between the upwelling and mesoscale eddies. The frontal dynamics is associated with ageostrophic circulation in the surface mixed layer, thus the generation of vertical velocities [21]. We compute the vertical velocity from the classical quasi-geostrophic ω-equation that reads:

$$\left(f^2 \partial_{zz} + N^2(z) \nabla^2\right) \omega = \boldsymbol{\nabla} \cdot \boldsymbol{\mathcal{Q}}\,, \tag{20}$$

with,

$$\boldsymbol{\mathcal{Q}} = \left[2f\left(\partial_x v \partial_z u + \partial_y v \partial_z v\right); -2f\left(\partial_x u \partial_z u + \partial_y u \partial_z v\right)\right]\,, \tag{21}$$

see Appendix A for details. Equation (20) is solved using a multigrid solver with Dirichlet boundary conditions. We used the quasi-geostrophic version of the ω-equation for its ease of implementation in the code and for its stability/convergence towards a solution (via the inversion of the Laplacian). Ref. [31] show in particular that the vertical velocity calculated with the semi-geostrophic omega equation (the Sawyer Eliassen equation) has the same direction as that calculated with the QG Omega equation. The maximal difference in intensity that these authors obtained for subsurface fronts was about 40%. The corresponding vertical velocities are drawn in grey contours in Figure 4. The vertical velocity intensified in the surface mixed layer is the signature of the secondary ageostrophic circulation associated with the frontal dynamics. The secondary ageostrophic circulation acts to bring back the isopycnals horizontally to restratify the upper mixed layer such that the geostrophic balance is restored. The horizontal turbulent fluxes of buoyancy and spiciness induced by the frontal dynamics are presented in Figure 4d,e. The spiciness is a variable whose isopycnal variations reflect isopycnal water-mass contrasts in density units [32]. The vertical turbulent fluxes are about two orders of magnitude weaker than the horizontal ones. Even though the horizontal and vertical circulation arising from the frontal interactions are triggered, the resulting sub-mesoscale features induces

turbulent fluxes mostly in the horizontal plane. The horizontal fluxes are maximal near the density and spiciness fronts. These eddy fluxes are cross- and down-gradient, but also, due to the presence of meanders and of transverse filaments, are along-gradients.

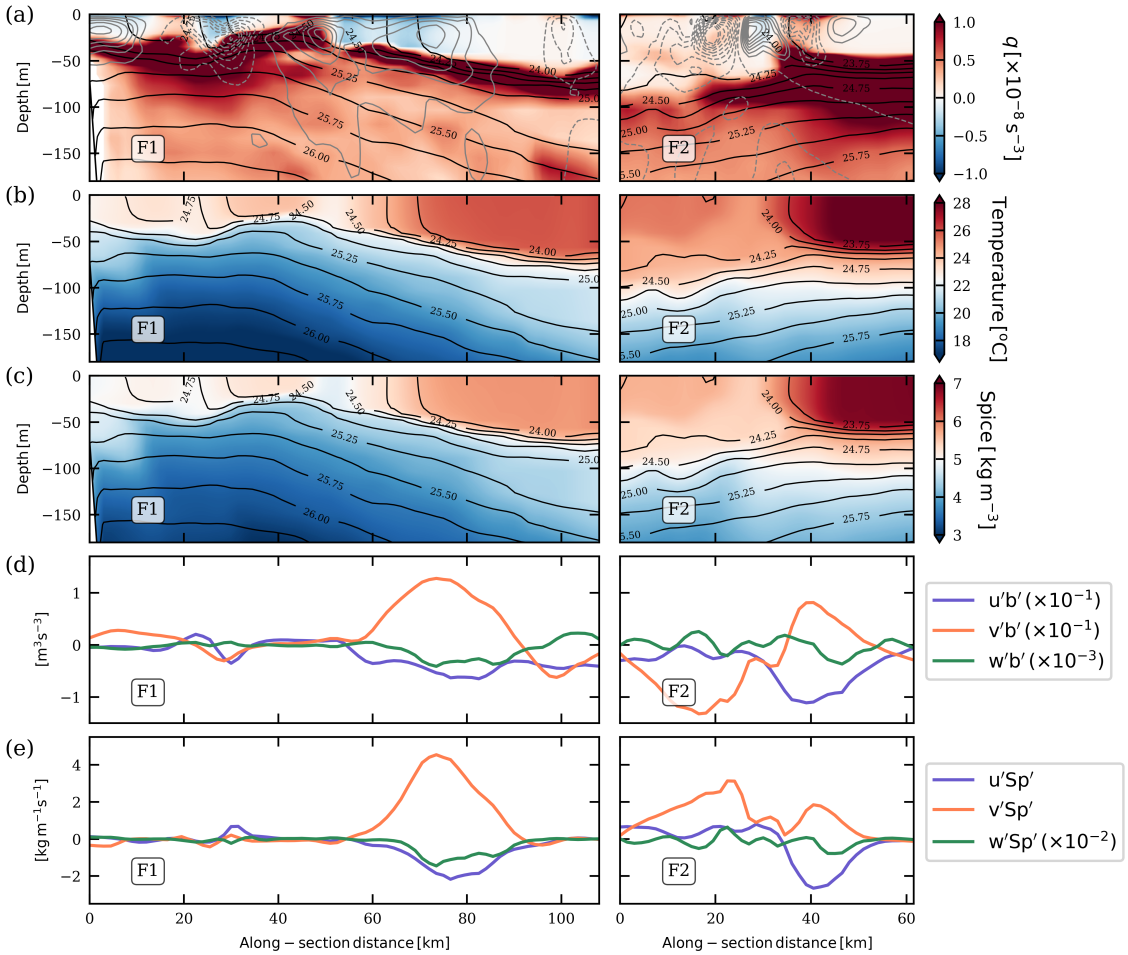

Figure 4. Vertical section of (**a**) Ertel potential vorticity, (**b**) temperature, (**c**) spiciness, and (**d**,**e**) buoyancy and spiceness turbulent fluxes integrated from the surface down to 50 m depth. (**a**–**c**) Density contours are drawn in black solid lines. (**a**) Grey contours stand for the vertical velocity computed from the ω-equation.

3.2. Surface Sub-Mesoscale Eddies Generation off the Cape of Ra'S al Hadd

During the spring intermonsoon, the OCC flows northward and forms a standing mesoscale anticyclonic eddy at the Cape of Ra's al Hadd (see Figure 5a,b). Off the Cape of Ra's al Hadd, sub-mesoscale eddies are also generated, subsequently advected by the standing mesoscale anticyclone (see inset in Figure 5a,b). Indeed, by flowing along the Omani coast, an intense shear layer (with opposite vorticity) is produced to cancel out the velocity at the coast. The OCC is intensified from the surface down to about 400 m depth; it is about 100 km wide, and its maximal horizontal velocity is about 1 m s^{-1} (see Figure 5c). At the Cape of Ra's al Hadd, the horizontal gradient of the Ertel potential vorticity ($\partial_y q$) of the OCC changes sign horizontally (see Figure 5d) from the surface down to 150 m depth. This is a necessary condition for horizontal shear instability to occur. The Horizontal Reynolds Stress (HRS), the Vertical Reynolds Stress (VRS), and the Vertical Buoyancy Flux (VBF) are calculated to indicate the dominant type of energy conversion. HRS and VRS are related to the conversion of mean to eddy kinetic energy through horizontal and vertical shear production, respectively. The eddy potential

to eddy kinetic energy is captured by VBF and is related to baroclinic instabilities. Following [33], the energy conversion terms are computed as:

$$\mathrm{HRS} = -\overline{\boldsymbol{u}'v'} \cdot \partial_y \overline{\boldsymbol{u}} - \overline{\boldsymbol{u}'u'} \cdot \partial_x \overline{\boldsymbol{u}}\,; \tag{22}$$

$$\mathrm{VRS} = -\overline{\boldsymbol{u}'w'} \cdot \partial_z \overline{\boldsymbol{u}}\,; \tag{23}$$

$$\mathrm{VBF} = \overline{w'b'}\,, \tag{24}$$

see Appendix B for details. These three terms are shown in Figure 5e. The HRS term prevails on the two other terms. It is maximum and positive on the southern side of the current. This confirms that the conversion of mean to eddy kinetic energy occurs through horizontal shear instability resulting in the formation of the sub-mesoscale cyclonic eddy off the Cape of Ra's al Hadd. The resulting sub-mesoscale eddy is about 15 km of radius and about 200 m thick.

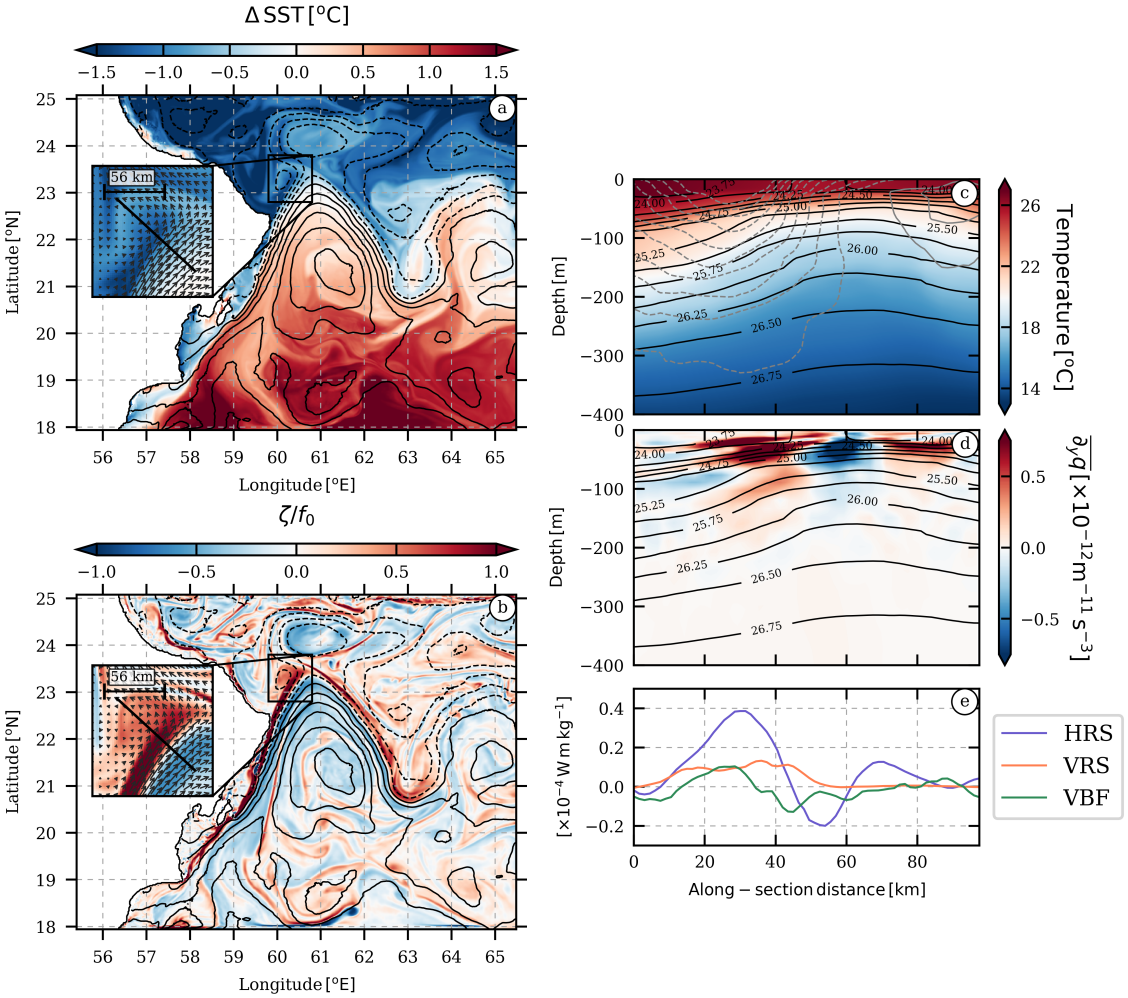

Figure 5. (**a**) Surface temperature anomaly and (**b**) surface relative vorticity normalized by the Coriolis frequency (f_0) during the Spring Intermonsoon. Black contours stand for the sea surface height anomaly. Surface velocity vectors are represented in insets. (**c**) Vertical section of temperature. Grey contours of cross-section component of the velocity and black contours of density are superimposed. (**d**) Vertical section of the horizontal gradient of Ertel potential vorticity. Black contours of density are superimposed. (**e**) Energy transfer terms averaged over 2 months and integrated from the surface down to 150 m depth.

3.3. Peddies Interaction with the Ra'S al Hadd Dipole

From the Strait of Hormuz on, PGOW flows in the Gulf of Oman as a slope current, between 200 and 300 m depth, following the northeastern Omani coast (the southern side of the Gulf of Oman). There, the pathways of PGOW are strongly influenced by the mesoscale eddy field. The current shear generated by these eddies can divert the PGOW outflow offshore and lead to the formation of sub-mesoscale eddies containing PGOW (commonly named a Peddy). During the summer monsoon, a sub-mesoscale eddy of PGOW was formed at the Cape of Ra's al Hamra, located upstream the Cape of Ra's al Hadd. The Peddy was then advected by the mean current along the northeastern Omani coast as shown in Figure 6 (1st column). The mean current was imposed by the cyclonic part of the standing Ra's al Hadd dipole. The temperature anomaly associated with the Peddy is about 2 °C regarding the surrounding water masses, and its relative vorticity reaches $0.5 f_0$. The maximal salinity trapped within the Peddy is about 36.6 psu. By considering the salinity anomaly with respect to the environment, the radius of the Peddy is about 10 km, that is below the deformation radius of the region ($R_d \sim 50$ km, from [34]), so that the Peddy is characterized as a sub-mesoscale eddy. Note the salinity value of the Peddy is much lower than that of the PGOW outflow at the Strait of Hormuz (about 40 psu) since the outflow undergoes efficient mixing performed by mesoscale eddies. Once the Peddy reaches the Cape of Ra's al Hadd, it is advected by the R'as al Hadd jet and wrapped around the anticyclonic eddy of the dipole (see Figure 6, 2nd and 3rd columns). Then, the Peddy becomes a filament of PGOW as shown in Figure 6 (4th column). The temperature anomaly decreases down to about 0.5 °C regarding the ambient water masses. The relative vorticity normalized by the areal average of the Coriolis frequency is now about 0.1. The vertical section of the filament indicates that the horizontal extent is about 10 km (about twice as small as that of the Peddy), while its thickness increases due to vertical stretching to the PV be materially conserved.

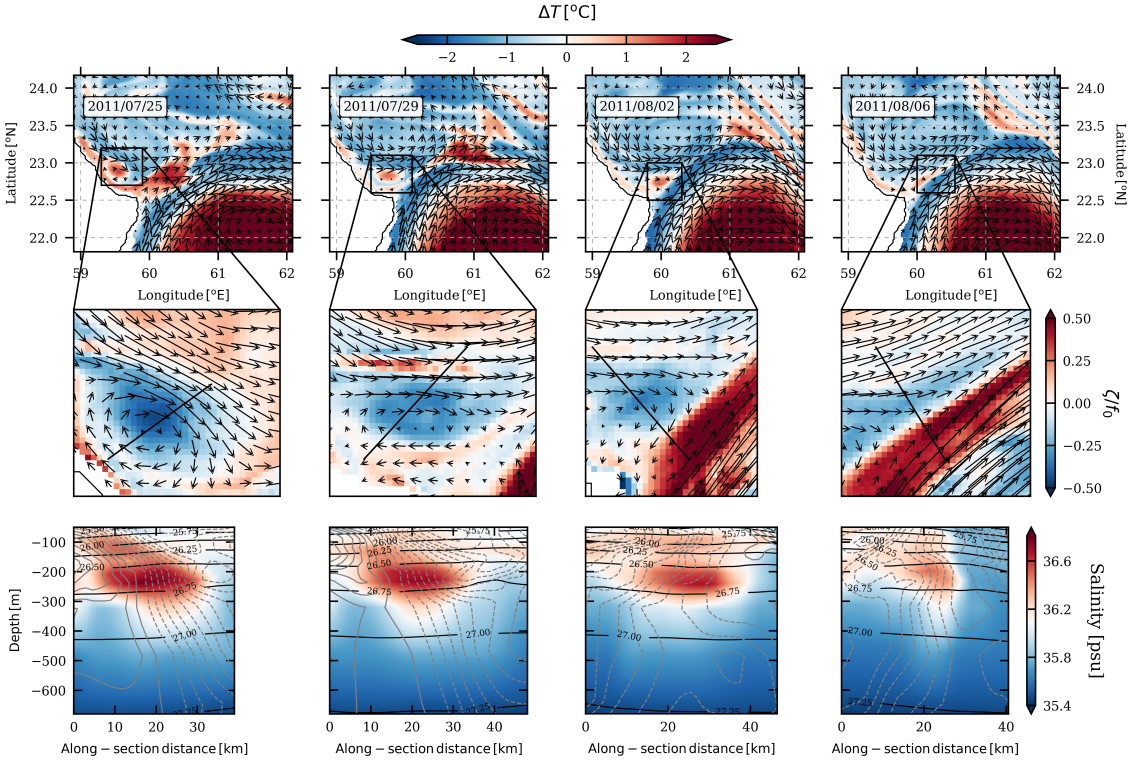

Figure 6. Time sequences of (**top panels**) temperature anomaly, (**middle panels**) relative vorticity normalized by the areal average of the Coriolis frequency at 250 m depth (arrows stand for the velocity vectors), and (**bottom panels**) vertical sections of (in colors) salinity, (in black contours) the density, and (in grey contours) the cross-section component of the velocity. The location of sections is drawn in middle panels in black solid lines.

We highlight the effect of the Ra's al Hadd jet stretching and shearing of sub-mesoscale eddies, by comparing the contributions of shear and strain to the relative vorticity of the dipole via the Okubo-Weiss parameter [35,36]:

$$\mathrm{OW} = S^2 - \zeta^2\,; \tag{25}$$

with $S^2 = (\partial_x u - \partial_y v)^2 + (\partial_x v + \partial_y u)^2$, the squared deformation rate. The filament of PGOW is associated with $\mathrm{OW} > 0$ (see Figure 7a), meaning that the strain prevails on the relative vorticity. The strain effect is induced by mesoscale eddies of the Ra's al Hadd dipole. The frontogenesis function is shown in Figure 7b. F_s is weak at the location of the filament of PGOW due to the weak horizontal density gradient because of the dilution of PGOW.

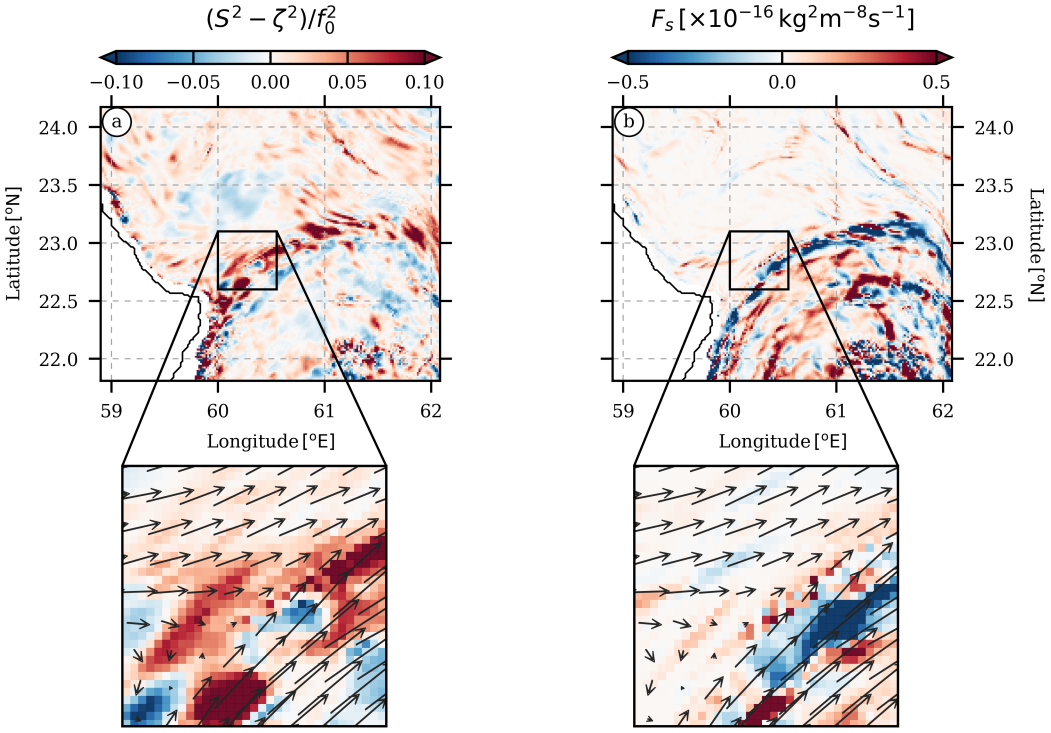

Figure 7. (**a**) Okubo-Weiss parameter and (**b**) frontogenesis function at 250 m depth. Arrows in insets stand for the velocity vector at 250 m depth.

3.4. Subsurface Sub-Mesoscale Eddies off the Southern Omani Coast

The OCC flows northward along the southern Omani coast during the summer monsoon. As mentioned above, the OCC is coupled then with an upwelling system. The cross-shore gradient of temperature is weaker at depth than at the surface but it still exists. At the surface, the maximal temperature anomaly is about 2 °C; at 360 m depth it reduces to 1 °C as shown in Figure 8a. In addition to the mesoscale eddies located of the Omani coast, sub-mesoscale anticyclone are produced at depth (see Figure 8b, and insets). The relative vorticity of such sub-mesoscale eddies is about $-0.5 f_0$. The energy transfer terms shown in Figure 8c in the cross-shore direction indicates that the OCC is baroclinically unstable in subsurface (i.e., VBF $\gg$ VRS $\sim$ HRS). However, the horizontal gradient of the Ertel potential vorticity changes sign both in the vertical and in the horizontal direction at depth (see Figure 8d). This indicates a mixed barotropic/baroclinic instability is also possible at intermediate depth (though the developed instability is presently essentially baroclinic). The instability develops in about 10 days. The vertical structure of the resulting sub-mesoscale eddy is shown in Figure 8e,f. The subsurface eddy is located at about 400 m depth with a radius of about 15 km and a vertical extent of 200 m depth.

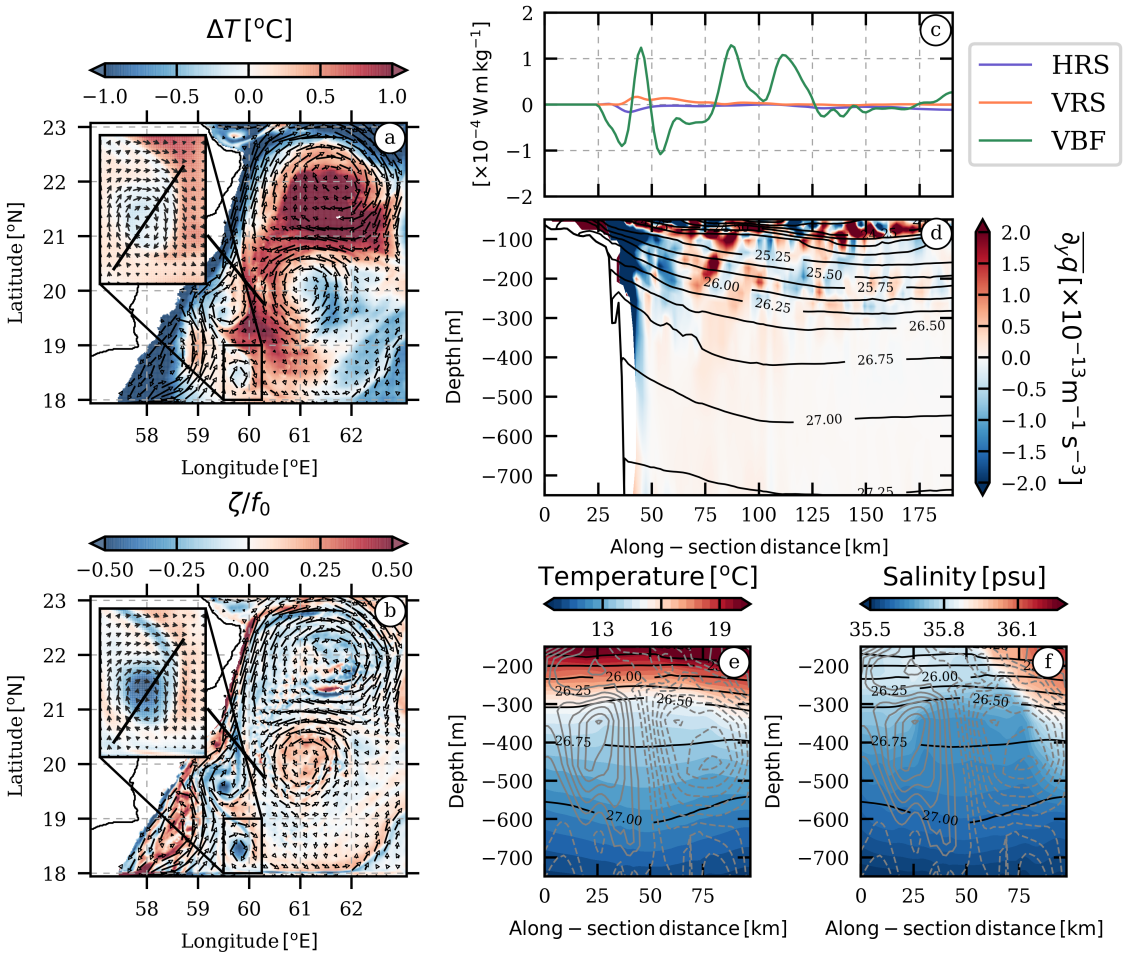

Figure 8. Dynamical structure of OCC at depth during the Summer monsoon. (**a**) Temperature anomaly and (**b**) surface relative vorticity normalized by the Coriolis frequency (f_0) at 360 m depth. Arrows stand for the velocity vectors. (**c**) Energy transfer terms averaged over a month and integrated from the surface down to 150 and 750 m depth and (**d**) vertical section of the horizontal gradient of Ertel potential vorticity averaged over a month. Contours of density are superimposed. (section drawn in panel (**a**,**b**)). (**e**,**f**) Vertical section of temperature and salinity. Contours of (black) density and (grey) cross-section velocity component are superimposed (section drawn in inset in panel (**a**,**b**)).

4. Summary and Conclusions

This paper has focused on the sub-mesoscale frontal dynamics in the northward Omani Coastal Current from May to September through the analysis of the HYCOM outputs. It has been shown that off the southern Omani coast, frontal dynamics are at play in the surface mixed layer as a result of the frontogenesis triggered by the interaction between the upwelling fronts and the mesoscale eddies. The ageostrophic circulation, the effect of the wind and the frontal stability have been studied. The interaction between the upwelling front and the neighboring mesoscale eddies leads to sub-mesoscale instabilities associated with ageostrophic motion and intense vertical velocities in the surface mixed layer during the south-west summer monsoon. During the spring intermonsoon, the OCC undergoes horizontal shear instabilities at the Cape of Ra's al Hadd resulting in the formation of sub-mesoscale eddies in the first hundred meters depth. The sub-mesoscale eddies of Persian Gulf Water (Peddies) produced during the summer monsoon and located below the thermocline, are driven and elongated by the intense strain rate imposed by the Ra's al Hadd jet. Thus, they contribute to the mixing of PGW at the mouth of the Gulf of Oman. Finally, subsurface sub-mesoscale eddies are also generated off the southern Omani coast as the result of baroclinic instabilities triggered by the

interaction of the mesoscale eddies with the upwelling system in summer. They are typically of 15 km width and 200 m thick.

Much remains to be studied. In particular, the generation and propagation of high-frequency waves has not been addressed here (see Appendix C). The breaking of such waves over the topography can lead to intense vertical mixing and to tall staircases in hydrological profiles near the southern Omani shelf (unpublished data). The interaction of the eddies with the Murray Ridge is another possible mechanism for the formation of small eddies and filaments in this region. These processes will be studied in future work.

Author Contributions: M.M. obtained and analyzed the results. M.M. and X.C. wrote the manuscript. All authors have read and agreed to the published version of the manuscript.

Funding: This research received no external funding.

Acknowledgments: MM was supported by a contract from SHOM "Validation du modele HYCOM sur la mer d'Arabie"; this work was done in partial fulfillment of the requirements for his PhD in physical oceanography. The authors thank Stephanie Correard and Remy Baraille for model outputs. The authors also thank Jonathan Gula for sharing its python's tools.

Conflicts of Interest: The authors declare no conflict of interest.

Appendix A. The Omega Equation

The omega equation has been obtained historically from the quasi-geostrophic and semi-geostrophic models. Geostrophy is the equilibrium between the Coriolis acceleration and the pressure gradient

$$u_g = -\frac{1}{\rho_0 f}\partial_y p = -\partial_y \psi\,, \tag{A1}$$

$$v_g = \frac{1}{\rho_0 f}\partial_x p = \partial_x \psi\,, \tag{A2}$$

where ψ is the geostrophic streamfunction.

Using hydrostatic balance, a relation, the thermal wind balance, is obtained between the vertical shear of horizontal velocity and the horizontal gradient of buoyancy:

$$f\partial_z u_g = -\partial_y b\,, \tag{A3}$$

$$f\partial_z v_g = \partial_x b \tag{A4}$$

In quasi-geostrophy, the geostrophic acceleration $(\partial_t + u_g\partial_x + v_g\partial_y)\boldsymbol{u}_g$ is re-instated near the Coriolis acceleration, in the horizontal momentum equations; this model is therefore quasi-bidimensional. In semi geostrophy, a more complete acceleration is used $(\partial_t + u\partial_x + v\partial_y + w\partial_z)\boldsymbol{u}_g$. The Omega equation is obtained from the equations of time evolution of geostrophic vorticity and of buoyancy; cross derivatives in z and x, y eliminate the time variation between them. Calling $N^2 = db/dz$ only for the static part of buoyancy, the equation obtained is

$$N^2(\partial_x^2 + \partial_y^2)w + f^2\partial_z w = -2\boldsymbol{\nabla}\cdot\boldsymbol{Q} \tag{A5}$$

where $\boldsymbol{Q}(-\partial_x\boldsymbol{u}_g\cdot\boldsymbol{\nabla}_h b, -\partial_y\boldsymbol{u}_g\cdot\boldsymbol{\nabla}_h b)$.

This equation is sometimes written for each of its components

$$N^2\partial_{xx}^2\psi + f^2\partial_{zz}\psi = -2Q_1 \tag{A6}$$

$$N^2\partial_{yy}^2\psi + f^2\partial_{zz}\psi = -2Q_2 \tag{A7}$$

In the semi-geostrophic case, the omega equation (also known as the Sawyer-Eliassen equation) contains more terms

$$N_s^2\partial_{xx}^2\psi - 2S^2\partial_{xz}\psi + F^2\partial_{zz}^2\psi = -2Q_1 \tag{A8}$$

for a front associated with a geostrophic current $v_g(x)$; here $N_s^2 = N^2 + \partial_z b$ where b is here the dynamic part of buoyancy, $S^2 = \partial_x b$, $F^2 = f(f + \partial_x v_g)$.

Appendix B. Energy Transfers

The energy equation and the energy transfers are computed by multiplying the momentum equations by the velocity to obtain the kinetic energy; the potential energy is ρgz for which the equation is obtained from buoyancy conservation.

In the absence of forcing and of dissipation, total energy (kinetic + potential) is conserved if there is no energy flux across the domain boundaries

$$\frac{D}{Dt}[\int dx \int dy \int dz\rho[(u^2 + v^2)/2 + gz] = 0\,. \tag{A9}$$

To compute energy transfers between the mean flow and its perturbation, a Reynolds decomposition of the variables is applied, e.g., $u = \overline{u} + u', v = \overline{v} + v', \rho = \rho + \rho'$, where the capital variables denote the mean flow and the primed variables, the perturbation.

Writing the energy equation for the perturbation

$$\frac{1}{2}\frac{D(u'^2 + v'^2)}{Dt} = -\boldsymbol{u'}u'\partial_x\overline{\boldsymbol{u}} - \boldsymbol{u'}v'\partial_y\overline{\boldsymbol{u}} - \boldsymbol{u'}w'\partial_z\overline{\boldsymbol{u}} + w'b'$$

This equation is then averaged over a wavelength of a perturbation. The right-hand side terms provide the Horizontal Reynolds Stress (HRS), the Vertical Reynolds Stress (VRS) and the vertical buoyancy flux (VBF). HRS is characteristic of the energy transfer from a mean flow which has a horizontal shear (in the case of a barotropic instability), VRS originates in the vertical shear of the flow (for Kelvin Helmholtz instability) and VBF is associated with baroclinic instability which displaces horizontally and vertically water masses with different densities.

Appendix C. High-Frequency Waves

The presence of the high-frequency waves are highlighted by decomposing the flow in a rotational and a divergent part (Helmholtz decomposition), as:

$$\boldsymbol{u} = \boldsymbol{u}_{\text{rot}} + \boldsymbol{u}_{\text{div}} = \boldsymbol{k} \times \boldsymbol{\nabla}\psi + \boldsymbol{\nabla}\chi\,. \tag{A10}$$

$\boldsymbol{u}_{\text{div}}$ is shown in Figure A1. Waves are generated along the southern Omani coast and by sub-mesoscale eddies resulting from the mixed barotropic/baroclinic instability. Our investigation of the high-frequency wave is limited by the model output saving frequency which is daily at depth. In space, the model solves internal waves for which:

$$\lambda > 2 \times c \times dt \tag{A11}$$

with λ the wavelength, c the wave phase speed, and $dt = 40\,\text{s}$ the model time step. For external waves $c = \sqrt{gH} = 0.4\,\text{m}\,\text{s}^{-1}$, with $g = 9.81\,\text{m}\,\text{s}^{-2}$ and $H = 2000\,\text{m}$. This gives $\lambda > 10\,\text{km}$. In time, the condition for solving the internal waves holds in the stratification frequency which is about $2 \times 10^{-3}\,s^{-1}$ corresponding to a period of 476 s. Since the model time step is 40 s, the model solves the internal waves in time. However, our daily model output is too coarse to perform further analysis on the high-frequency waves.

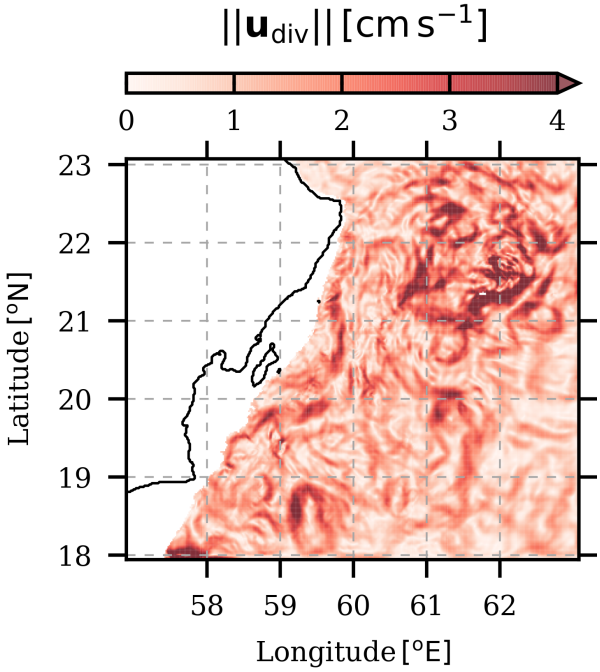

Figure A1. Divergent part of the velocity computed on the same day as in Figure 8 at 360 m depth.

References

1. Schott, F.A.; McCreary, J.P., Jr. The monsoon circulation of the Indian Ocean. *Prog. Oceanogr.* **2001**, *51*, 1–123. [CrossRef]
2. Defant, A. *Physical Oceanography*; Pergamon Press: New York, NY, USA, 1961; Volume 1.
3. Shi, W.; Morrison, J.M.; Böhm, E.; Manghnani, V. The Oman upwelling zone during 1993, 1994 and 1995. *Deep. Sea Res. Part II Top. Stud. Oceanogr.* **2000**, *47*, 1227–1247. [CrossRef]
4. Flagg, C.N.; Kim, H.S. Upper ocean currents in the northern Arabian Sea from shipboard ADCP measurements collected during the 1994–1996 US JGOFS and ONR programs. *Deep. Sea Res. Part II Top. Stud. Oceanogr.* **1998**, *45*, 1917–1959. [CrossRef]
5. De Marez, C.; l'Hégaret, P.; Morvan, M.; Carton, X. On the 3D structure of eddies in the Arabian Sea. *Deep. Sea Res. Part I Oceanogr. Res. Pap.* **2019**, *150*, 103057. [CrossRef]
6. L'Hégaret, P.; Duarte, R.; Carton, X.; Vic, C.; Ciani, D.; Baraille, R.; Corréard, S. Mesoscale variability in the Arabian Sea from HYCOM model results and observations: Impact on the Persian Gulf Water path. *Ocean. Sci.* **2015**, *11*, 667.
7. Pous, S.; Lazure, P.; Carton, X. A model of the general circulation in the Persian Gulf and in the Strait of Hormuz: Intraseasonal to interannual variability. *Cont. Shelf Res.* **2015**, *94*, 55–70. [CrossRef]
8. Bower, A.S.; Hunt, H.D.; Price, J.F. Character and dynamics of the Red Sea and Persian Gulf outflows. *J. Geophys. Res. Ocean.* **2000**, *105*, 6387–6414. [CrossRef]
9. Pous, S.; Carton, X.; Lazure, P. Hydrology and circulation in the Strait of Hormuz and the Gulf of Oman—Results from the GOGP99 Experiment: 1. Strait of Hormuz. *J. Geophys. Res. Ocean.* **2004**, *109*, 42–56. [CrossRef]
10. Pous, S.; Carton, X.; Lazure, P. Hydrology and circulation in the Strait of Hormuz and the Gulf of Oman—Results from the GOGP99 Experiment: 2. Gulf of Oman. *J. Geophys. Res. Ocean.* **2004**, *109*. [CrossRef]
11. Carton, X.; L'Hegaret, P.; Baraille, R. Mesoscale variability of water masses in the Arabian Sea as revealed by ARGO floats. *Ocean. Sci.* **2012**, *8*, 227–248. [CrossRef]
12. L'Hégaret, P.; Carton, X.; Louazel, S.; Boutin, G. Mesoscale eddies and submesoscale structures of Persian Gulf Water off the Omani coast in spring 2011. *Ocean. Sci.* **2016**, *12*. [CrossRef]
13. Mensa, J.A.; Garraffo, Z.; Griffa, A.; Özgökmen, T.M.; Haza, A.; Veneziani, M. Seasonality of the submesoscale dynamics in the Gulf Stream region. *Ocean. Dyn.* **2013**, *63*, 923–941. [CrossRef]

14. Gula, J.; Molemaker, M.J.; McWilliams, J.C. Submesoscale cold filaments in the Gulf Stream. *J. Phys. Oceanogr.* **2014**, *44*, 2617–2643. [CrossRef]
15. Gula, J.; Molemaker, M.J.; McWilliams, J.C. Submesoscale dynamics of a Gulf Stream frontal eddy in the South Atlantic Bight. *J. Phys. Oceanogr.* **2016**, *46*, 305–325. [CrossRef]
16. Nagai, T.; Tandon, A.; Yamazaki, H.; Doubell, M.J. Evidence of enhanced turbulent dissipation in the frontogenetic Kuroshio Front thermocline. *Geophys. Res. Lett.* **2009**, *36*. [CrossRef]
17. Rocha, C.B.; Gille, S.T.; Chereskin, T.K.; Menemenlis, D. Seasonality of submesoscale dynamics in the Kuroshio Extension. *Geophys. Res. Lett.* **2016**, *43*, 11–304. [CrossRef]
18. Krug, M.; Swart, S.; Gula, J. Submesoscale cyclones in the Agulhas current. *Geophys. Res. Lett.* **2017**, *44*, 346–354. [CrossRef]
19. Tedesco, P.; Gula, J.; Ménesguen, C.; Penven, P.; Krug, M. Generation of submesoscale frontal eddies in the Agulhas Current. *J. Geophys. Res. Ocean.* **2019**. [CrossRef]
20. Capet, X.; McWilliams, J.C.; Molemaker, M.J.; Shchepetkin, A. Mesoscale to submesoscale transition in the California Current System. Part I: Flow structure, eddy flux, and observational tests. *J. Phys. Oceanogr.* **2008**, *38*, 29–43. [CrossRef]
21. Capet, X.; McWilliams, J.C.; Molemaker, M.J.; Shchepetkin, A. Mesoscale to submesoscale transition in the California Current System. Part II: Frontal processes. *J. Phys. Oceanogr.* **2008**, *38*, 44–64. [CrossRef]
22. Capet, X.; McWilliams, J.C.; Molemaker, M.J.; Shchepetkin, A. Mesoscale to submesoscale transition in the California Current System. Part III: Energy balance and flux. *J. Phys. Oceanogr.* **2008**, *38*, 2256–2269. [CrossRef]
23. Meunier, T.; Barton, E.D.; Barreiro, B.; Torres, R. Upwelling filaments off Cap Blanc: Interaction of the NW African upwelling current and the Cape Verde frontal zone eddy field? *J. Geophys. Res. Ocean.* **2012**, *117*. [CrossRef]
24. Chassignet, E.P.; Hurlburt, H.E.; Smedstad, O.M.; Halliwell, G.R.; Hogan, P.J.; Wallcraft, A.J.; Baraille, R.; Bleck, R. The HYCOM (hybrid coordinate ocean model) data assimilative system *J. Mar. Sys.* **2007**, *65*, 60–83. [CrossRef]
25. Morvan, M.; L'Hégaret, P.; de Marez, C.; Carton, X.; Corréard, S.; Baraille, R. Life cycle of mesoscale eddies in the Gulf of Aden. *Geophys. Astrophys. Fluid Dyn.* **2020**, 1–19. [CrossRef]
26. Debreu, L.; Vouland, C.; Blayo, E. AGRIF: Adaptive grid refinement in Fortran. *Comput. Geosci.* **2008**, *34*, 8–13. [CrossRef]
27. Large, W.G.; McWilliams, J.C.; Doney, S.C. Oceanic vertical mixing: A review and a model with a nonlocal boundary layer parameterization. *Rev. Geophys.* **1994**, *32*, 363–403. [CrossRef]
28. Hoskins, B.J. The mathematical theory of frontogenesis. *Annu. Rev. Fluid Mech.* **1982**, *14*, 131–151. [CrossRef]
29. Hoskins, B.J.; Bretherton, F.P. Atmospheric frontogenesis models: Mathematical formulation and solution. *J. Atmos. Sci.* **1972**, *29*, 11–37. [CrossRef]
30. Thomas, L.N.; Lee, C.M. Intensification of ocean fronts by down-front winds. *J. Phys. Oceanogr.* **2005**, *35*, 1086–1102. [CrossRef]
31. Siegelman, L.; Klein, P.; Rivière, P.; Thompson, A.F.; Torres, H.S.; Flexas, M.; Menemenlis, D. Enhanced upward heat transport at deep submesoscale ocean fronts. *Nat. Geosci.* **2020**, *13*, 50–55. [CrossRef]
32. McDougall, T.J.; Krzysik, O.A. Spiciness. *J. Mar. Res.* **2015**, *73*, 141–152. [CrossRef]
33. Gula, J.; Molemaker, M.J.; McWilliams, J.C. Topographic generation of submesoscale centrifugal instability and energy dissipation. *Nat. Commun.* **2016**, *7*, 12811. [CrossRef] [PubMed]
34. Chelton, D.B.; Deszoeke, R.A.; Schlax, M.G.; El Naggar, K.; Siwertz, N. Geographical variability of the first baroclinic Rossby radius of deformation. *J. Phys. Oceanogr.* **1998**, *28*, 433–460. [CrossRef]
35. Okubo, A. Horizontal dispersion of floatable particles in the vicinity of velocity singularities such as convergences. In *Deep Sea Research and Oceanographic Abstracts*; Elsevier: Amsterdam, The Netherlands, 1970; Volume 17, pp. 445–454.
36. Weiss, J. The dynamics of enstrophy transfer in two-dimensional hydrodynamics. *Physica D* **1991**, *48*, 273–294. [CrossRef]